Calibration and artifact correction in an angular-domain fluorescence optical projection tomography system

Torres, Veronica, Li, Chengyue, Zhou, Wei, Brankov, Jovan, Tichauer, Kenneth

Veronica C. Torres, Chengyue Li, Wei Zhou, Jovan G. Brankov, Kenneth M. Tichauer, "Calibration and artifact correction in an angular-domain fluorescence optical projection tomography system," Proc. SPIE 11633, Design and Quality for Biomedical Technologies XIV, 116330K (5 March 2021); doi: 10.1117/12.2584737

Event: SPIE BiOS, 2021, Online Only

Calibration and artifact correction in an angular-domain fluorescence optical projection tomography system

Veronica C. Torres*[a], Chengyue Li[a], Wei Zhou[a], Jovan G. Brankov[b], Kenneth M. Tichauer[a]
[a]Department of Biomedical Engineering, Illinois Institute of Technology, 3255 S Dearborn St., Chicago, IL USA 60616; [b]Department of Electrical and Computer Engineering, Illinois Institute of Technology, 3255 S Dearborn St., Chicago, IL USA 60616

ABSTRACT

Fluorescence optical projection tomography with angular restriction is a promising technique for mesoscopic imaging of low scattering biological samples. As such, an angular domain system is being developed to address the problem of undetected micrometastases in lymph node biopsy tissues. Previous studies demonstrated its utility for lymph node applications and rigorously characterized imaging performance of the system. Through this evaluation, image artifacts were revealed in the reconstructions that limit achievable contrast and resolution. The objective of this work was to investigate the cause of those artifacts and potential remedies. Results demonstrated that an incorrect axis of rotation and detector response were the significant contributors of image artifacts, but post-acquisition calibration could account for the errors.

Keywords: tomographic reconstruction, optical projection tomography, angular domain, fluorescence, lymph node

1. INTRODUCTION

Optical projection tomography (OPT) has been used extensively for 3D visualization of biological specimens. Whole small animal organs and embryos have been imaged in high resolution to provide functional information and maps of gene expression.[1-3] OPT, however, remains limited because it relies on optically clear samples; whether that be inherently transparent like zebrafish and embryos, or from chemical treatment with clearing agents. Therefore, when clearing is not possible, images suffer from blur.

It was demonstrated that angular domain imaging is one method capable of improving resolution in intact, turbid samples. With this technique, scattered light can be rejected via angular array filtering[4], or as demonstrated in previous work through simulation[5] and experiment[6], via pinhole in a bi-telecentric lens system. Strict angular restriction (NA = 0.005) was implemented in an angular domain early photon tomography (ADEPT) system, that enabled detection and localization of ~200 µm diameter fluorescence inclusions in 1 cm lymph nodes. This promising demonstration prompted further investigation into the capabilities of the system and options for improvement. The ADEPT was characterized in terms of depth of focus, geometric and fluorescence reconstruction accuracy, and detection sensitivity.[7] Findings of these previous studies suggested the need for system calibration, and as such, this work investigates the causes of those image artifacts along with potential solutions.

2. METHODS

2.1 System overview

A full description of the system is detailed in previous work[7], but a noteworthy change that was made between the first and second generation system is upgrading the light sources from the more costly femto- and picosecond pulsed lasers to low-cost light emitting diodes (LEDs). This improves the maximum output power by about 100 times, which has the advantage of increasing the number of collected weakly scattered photons, thereby reducing imaging time (a concern especially with implementation of strict angular restriction). In addition, by transitioning from a source with high inherent spatial coherence to low, speckle artifacts can be reduced. A schematic of the system with these light sources are shown in Fig. 1(a). Briefly, the system employs 660 nm and 780 nm continuous wave LED sources that are collimated to an illumination spot size of ~2.5 cm. Samples are embedded in transparent agarose gel cylinders, then glued to a rod on a 2-

Design and Quality for Biomedical Technologies XIV, edited by Jeeseong Hwang, Gracie Vargas, Proc. of SPIE Vol. 11633, 116330K · © 2021 SPIE · CCC code: 1605-7422/21/$21 · doi: 10.1117/12.2584737

axis motorized translation and rotation stage that is suspended above a custom-made optical cell, which acts as an index-matching bath. Angle-restricted imaging was achieved with an iris diaphragm of 12 mm diameter placed within a telecentric lens system, lending a NA of 0.01. Detection was achieved with a 16-bit sCMOS (Quantalux, Thorlabs). Fluorescence imaging was performed as shown in Fig. 1(b), and transmission-based tomography was carried out in the same way with the exception of the filters.

Transmission- and fluorescence-based tomography was performed on the ADEPT system where images were collected in 5° intervals over 360° for a total of 72 projections each. Camera exposure time for each projection was 0.1 s and 2 s for all transmittance-based and fluorescence imaging, respectively. Image reconstruction was done using a simple filtered backprojection (FBP) algorithm, and was implemented with Matlab's built-in inverse Radon transform. Absorption images were reconstructed from transmission-based datasets using the relationship $A = -\log_{10}T$, where A is the absorbance and T is the transmittance; and fluorescence reconstructions were performed directly on the collected emission intensity images.

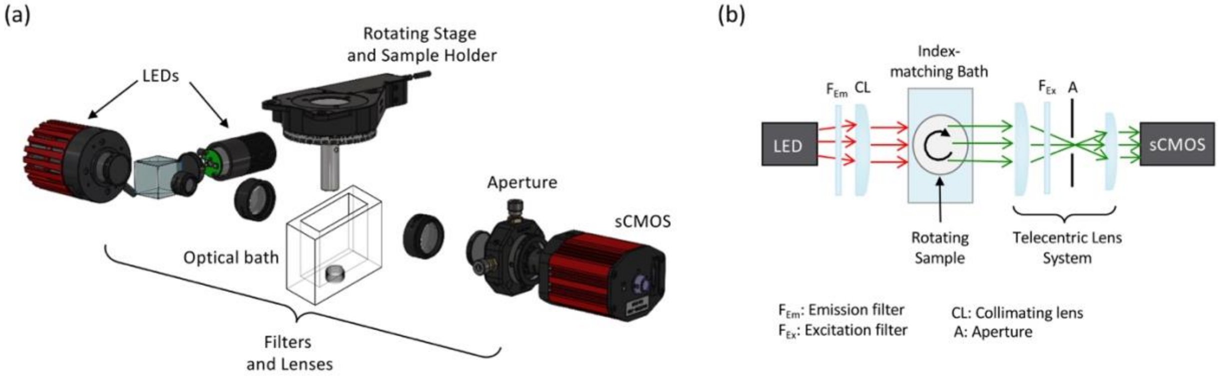

Figure 1. (a) System schematic. (b) Top down view of the fluorescence-based tomography setup.

2.2 Axis of rotation correction

Artifacts arise when reconstructing off-axis data sets because the back-projection algorithm assumes that the center of rotation is the center of the projections. Although the sample-holding rod in the system is aligned as closely as possible to the center of the field of view (FOV) prior to image acquisition, the exact position of the rotational axis is not always well known, and experimental error may add some deviation. Because of this, the center of rotation needs to be corrected for post-acquisition. Rather than trying to find the actual center of rotation, a virtual rotational axis was created that could account for translation and vertical tilt. This worked using two assertions: 1) when an object (and its axis of rotation) is moved in real space, the sinogram will also move, but the pattern will remain unchanged; and 2) a point on the object follows a circular trajectory around the axis of rotation (AoR), and a sinusoidal function on the sinogram when the object is rotated.[8] Therefore, if a fixed point can be tracked throughout its rotation, the sinogram can be corrected such that the midline of the sinusoidal curve becomes the center line (virtual axis of rotation). Changing the sinogram in this manner had the same effect as centering the object in real space. This method works well for known symmetrical objects, like cylinders, but for more complex or unknown shapes, it may be difficult to track a fixed point or know the expected ideal sinogram pattern. In that case, the adjusted axis of rotation was determined by stepping through different assumed centers of rotation, and finding the point where variance of the reconstructed image was maximum. This "autofocus" technique makes use of the idea that off-axis data reconstructions are a convolution of the correct image and a blurring function; therefore, the least blurry reconstruction would be closest to the true image and have the greatest variance.[9] The methods described above account only for translation error in 2D. While the same technique could be applied to each transverse slice independently to account for tilt of the rotational axis, it would be rather time consuming. Instead, the axis of rotation correction was done for two arbitrary rows selected from the projection images – one near the top of the sample, and the other near the bottom. Intermediate positions of the rotational axis were then interpolated by fitting a line through the two determined points.

2.3 Test phantoms and experiments

To test the AoR calibration methods, two phantoms were used, each made up of a ~12.5 mm diameter transparent agarose (1% w/v) cylinder bulk: one with a single 0.7 mm diameter graphite rod set diagonally [Fig. 2(a)] and another with eight

0.7 mm graphite rods set in a spiral orientation. Transmission-based tomography was performed on the ADEPT system for both. To assess reconstruction for single-intensity inclusions in transmission-mode, the same spiral phantom described above was used. The rods served as optical absorbers to create contrast. Fluorescence reconstruction performance with variable intensity inclusions was tested using the same bulk agarose phantom composition, but three ~1.15 mm inner-diameter glass capillary tubes, each with a different concentration (0.1 µM, 1 µM, and 10 µM) of IRDye-680RD were embedded. All samples were submerged in a water bath for index-matching, and ADEPT tomography was performed. Note, these experiments were carried out for both light sources (700 nm and 800 nm channels), but data using only one channel is shown because results were similar.

3. RESULTS AND DISCUSSION

Left uncorrected, the FBP algorithm used assumes the AoR is the center of the projection's FOV. For the collected data with the full FOV, this was the 960th column of pixels [yellow dashed line in Fig. 2(c)]. Immediately, it can be seen from opposite projections (0˚ in green and 180˚ in magenta) that that axis was not at the midline between the two inclusion views. The effects were illustrated in Fig. 2(d). Three slices were fully reconstructed – the first, middle and last blue dashed lines in Fig. 2(b) – and double edge artifacts were noticeably present. This was shown in the horizontal and vertical line profile plots across the inclusion where one large peak between two smaller peaks were observed. Zoomed-in contour plots of the reconstructions of these inclusion regions were produced for all five slices indicated in Fig. 2(b), and they also clearly illustrate double edge artifacts. Since the graphite rod was cylindrical in shape and the expected sinogram pattern was known, fixed point tracking was used to correct for AoR translation in slices at the top and bottom of the sample, and the resultant line used as the corrected AoR was z = 0.0072x + 926.6353 [solid yellow line in Fig. 2(c)]. The reconstructed results are shown in Fig. 2(e) where the double edge artifacts are no longer present and the large peaks in the profile plots eliminated. These results provided confidence in applying the technique for subsequent reconstructions.

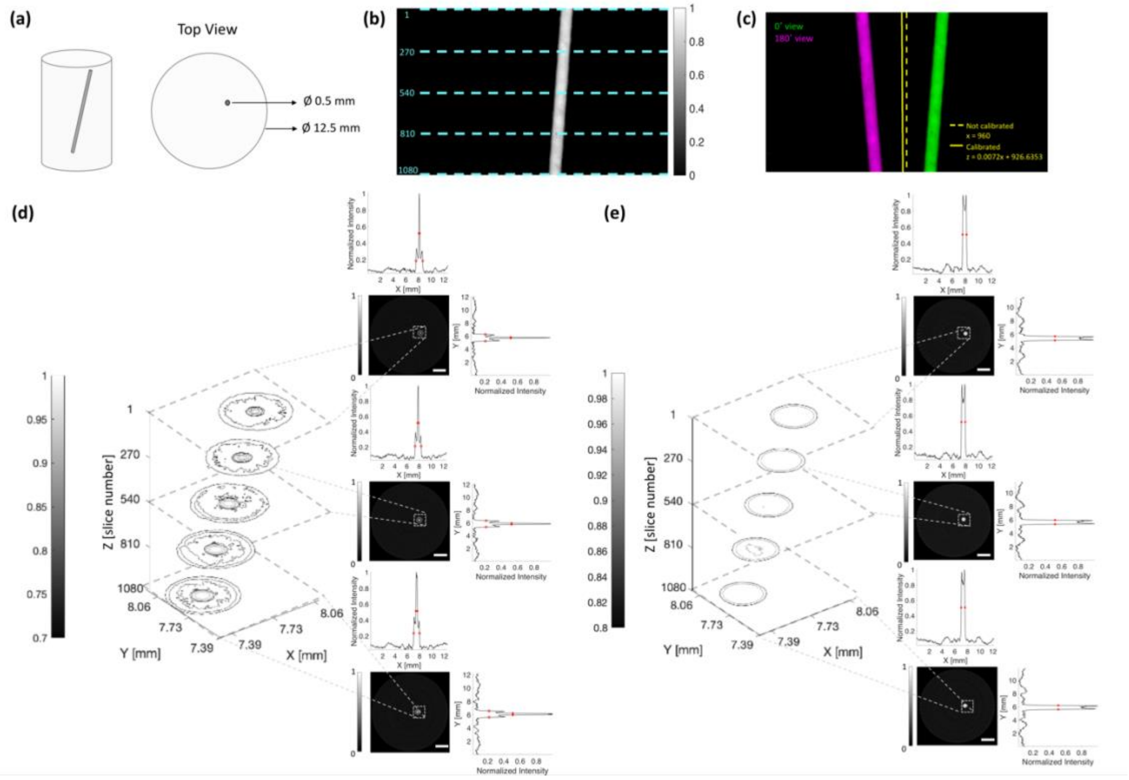

Figure 2. Axis of rotation (AoR) correction using fixed point tracking. (a) Phantom geometry. (b) Representative projection with reconstructed slices indicated by the blue dashed lines. (c) Projection views at 0˚ (green) and 180˚ (magenta) with uncorrected (yellow dashed line) and corrected (yellow solid line) rotational axes. (d) Uncorrected AoR and corrected (e) reconstructed slices with horizontal and vertical line profile plots through the inclusion, and contour plots of the inclusion region. Scale bars are 2 mm.

While it was possible to use fixed point tracking for the phantom above, it is not as useful for more complex samples where a point of interest cannot be followed or the expected sinogram is unknown. For such situations, the "autofocus" technique described above can be applied. This was tested on a phantom with multiple graphite rods arranged in a spiral formation. Figure 3(a) illustrates the ADEPT reconstruction without AoR calibration and significant double edge artifacts can be seen; however, after employing the autofocus method where a new, virtual center of rotation was applied based on measures of maximum total image variance, the reconstruction was visibly improved [Fig. 3(b)]. The results were also validated against reconstructions produced from a microCT scan [Fig. 3(c)], and an overlay of the detected inclusions from both modalities showed good agreement in spatial overlap [Fig. 3(d)]. Furthermore, successful implementation of the AoR correction with this technique was confirmed from volumetric reconstruction of the object. As shown in Figure 3(e), slices along the entire length of the inclusions were reconstructed with no artifacts demonstrating that an AoR can be estimated using only two slices. These results of AoR calibration illustrated the importance of correctly aligning samples prior to image acquisition in order to minimize error, as rather significant artifacts can arise from misalignment; but it was also proven that the deviation can be accounted for with confidence post acquisition.

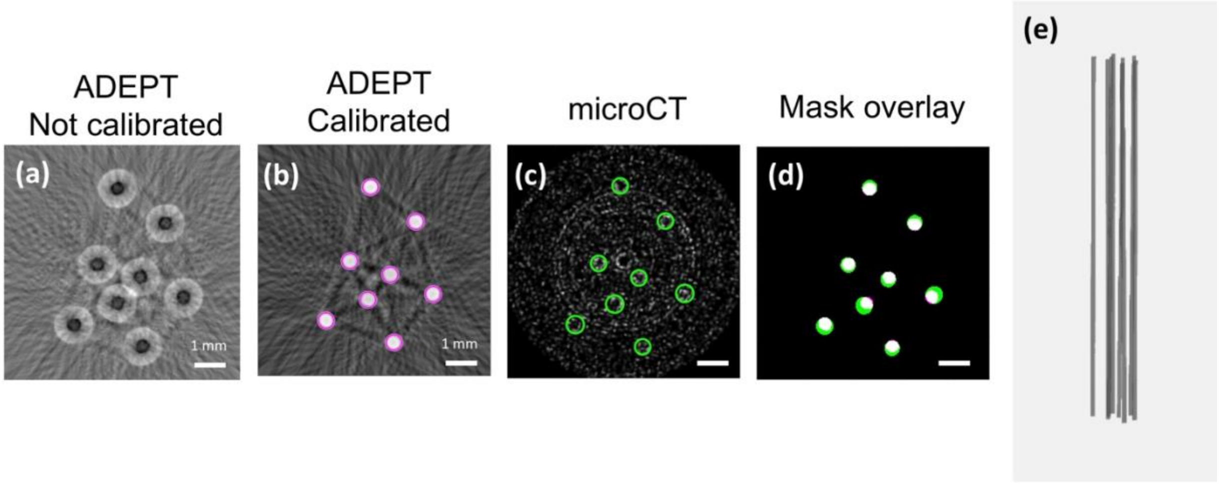

Figure 3. Axis of rotation (AoR) correction using an "autofocus" technique. (a) Uncorrected AoR and (b) corrected AoR reconstructed slices of a transverse slice through transparent agarose phantom embedded with eight graphite rods arranged in a spiral formation. (c) microCT reconstruction. (d) Overlay of masked ADEPT (magenta) and microCT (green) reconstructions. White indicates regions of overlap. (e) Isosurface volumetric reconstruction from ADEPT scanned data.

Streak artifacts were also revealed in the ADEPT data, both in the uncalibrated and calibrated reconstructions. These appeared along ray paths along high intensity regions, and can be attributed to nonlinear detector response and pixel-to-pixel variability. The following simulations were conducted to prove that the observed streak artifacts were indeed caused by the detector. A masked image of the detected objects from an ADEPT reconstructed slice was used as a phantom; the inclusions and background were assigned absorption values equal to the mean of the associated regions in the ADEPT slice [Fig. 4(b)]. Projection data was simulated by calculating the Radon transform of the phantom image. First, the number of collected projections was varied to determine if the streaks were coming from missing data (second row of Fig. 4). With the same rotational increment between acquisitions ($\Delta\theta = 5^\circ$), the simulated result was very similar to the actual ADEPT reconstruction [Fig. 4(a)], but without the streak artifacts. Increasing $\Delta\theta$ to 10° also produced more streaks, however not in the characteristic pattern observed. Decreasing the increment to 1° on the other hand, generated very clear artifact-free data, demonstrating that more projections does remove artifacts (a promising finding to implement in future experiments), but likely does not affect the patterned line paths connecting the inclusions.

Bad pixel, and nonlinear detector response and pixel-to-pixel variability were simulated following the procedure described in.[9] Figure 4(g,h) reveals ring artifacts that arise from bad pixels – those that have a response very different from the rest of the detector. Despite increasing the number of projections from every 5° to 1°, the artifacts remained, unlike in the "noise-free linear" detector scenario where the errors were easily eliminated by simply collecting more data. A similar finding was observed in the addition of detector nonlinearity and variability (last row of Fig. 4). The streak artifacts seen in the experimental data were reproduced, where the $\Delta\theta = 5^\circ$ simulated image [Fig. 4(i)] was strikingly similar to the actual

ADEPT image [Fig. 4(a)]. Therefore, as proven by Walls et al.[9], with proper calibration of the detector, the reverse of what was implemented in these simulations can be applied to the experimental data, and the streak artifacts avoided.

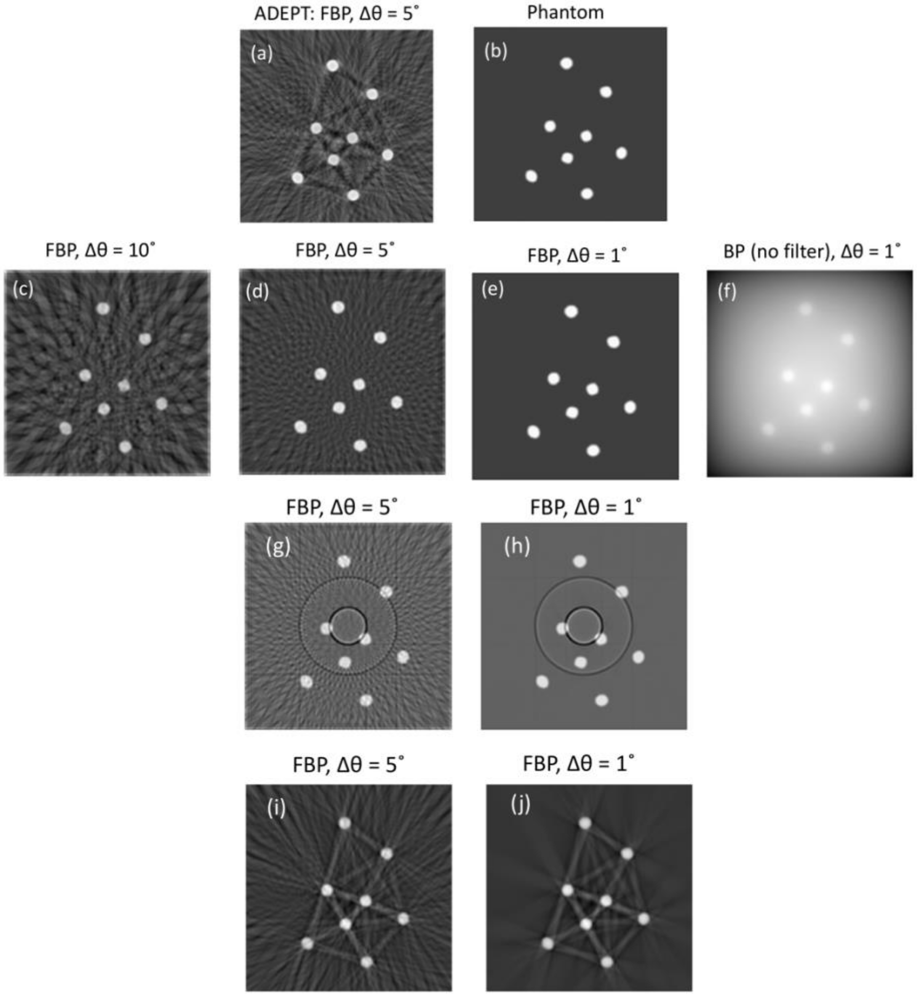

Figure 4. Bad pixel and nonlinear detector response reconstruction artifact simulations for single intensity inclusions. (a) ADEPT reconstruction from experimental physical phantom. (b) Simulated phantom mimicking measured data from (a). (c)-(f) Reconstructions of the simulated phantom in (b) using an "ideal" detector for different number of collected projections and methods. Reconstructions of the simulated phantom using a detector with (g,h) "bad" or dead pixels and (i,j) nonlinear response and pixel-to-pixel variability.

A representative ADEPT-generated fluorescence reconstruction of the variable concentration fluorescent phantom is show in Fig. 5(a). As expected, three inclusions were observed with varying intensity; however, contrast and resolution were affected by streak artifacts. Since the artifacts revealed in the fluorescence phantoms were comparable to those that appeared in the graphite phantoms, it was hypothesized that the source of error was the same, and the streaks could be reproduced through simulation again. Whereas the graphite phantom was of single absorption intensity, this fluorescent phantom included varying levels of signal, owing to the differences in added dye concentration. The simulation was generated in the same manner as described above. Fluorescent inclusions were given intensities increasing over a 2-order-of-magnitude range. Again, artifacts in the reconstructions of Fig. 5(c) and (d) for "ideal" detectors were only present because of missing data from fewer projections. Not until the detector response was altered in the second row [Fig. 5(e) and (f)] did the expected streak artifacts become visible and sustained. It is important to note how the size and intensity of the streaks changed along their path based on signal. This may help explain why the inclusions with lower concentration were harder to detect.

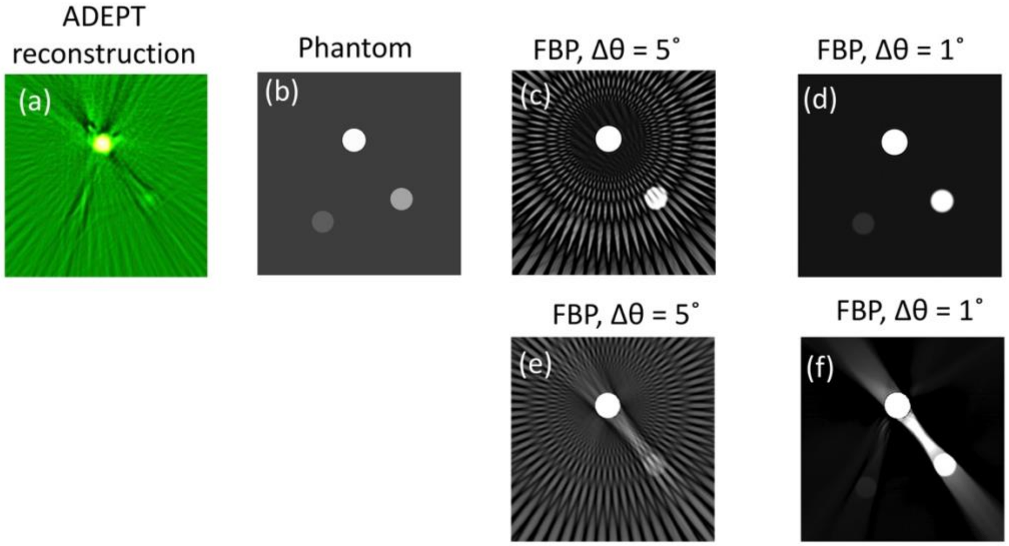

Figure 5. Bad pixel and nonlinear detector response reconstruction artifact simulations for variable intensity inclusions. (a) ADEPT reconstruction from experimental phantom. (b) Simulated phantom mimicking measured data from (a). Reconstructions of the simulated phantom using a detector (c,d) with "bad" or dead pixels and (e,f) nonlinear response and pixel-to-pixel variability for different number of collected projections.

4. CONCLUSION

The importance of system and detector calibration in transmission- and fluorescence-based optical projection tomography was demonstrated here. Previous work characterized such a system for angular-domain imaging where image artifacts were prevalent when calibration was not implemented. It was shown that an incorrect axis of rotation, bad detector pixels, and nonlinear detector response and pixel-to-pixel variability result in double edge artifacts, ring artifacts, and streak artifacts, respectively, in reconstructed images. Left uncorrected, these factors have the potential to dramatically hinder image quality, but as shown here, post-acquisition techniques can account for these errors. This understanding will help guide future design and imaging procedures of the developed ADEPT system.

REFERENCES

[1] T. Alanentalo, A. Asayesh, H. Morrison, C.E. Lorén, D. Holmberg, J. Sharpe, and U. Ahlgren., "Tomographic molecular imaging and 3D quantification within adult mouse organs," Nature methods, vol. 4, no. 1, pp. 31-33, (2007).

[2] A.U. Eriksson, C. Svensson, A. Hörnblad, A. Cheddad, E. Kostromina, M. Eriksson, N. Norlin, A. Pileggi, J. Sharpe, F. Georgsson, T. Alanentalo, U. Ahlgren, "Near Infrared Optical Projection Tomography for Assessments of β-cell Mass Distribution in Diabetes Research," J. Vis. Exp. (71), e50238, doi:10.3791/50238 (2013).

[3] J. Sharpe, "Optical Projection Tomography," Annu. Rev. Biomed. Eng. 2004. 6:209–28 doi: 10.1146/annurev.bioeng.6.040803.140210, (2004).

[4] F. Vasefi, "Advancements in Angular Domain Optical Imaging in Biological Tissue," Doctor of Philosophy, Faculty of Applied Sciences, Simon Fraser University, Simon Fraser University Library, 2010.

[5] L. Sinha, F. Massanes, V. C. Torres, C. Li, K. M. Tichauer, and J. G. Brankov, "Comparison of time- and angular-domain scatter rejection in mesoscopic optical projection tomography: a simulation study," Biomed Opt Express, vol. 10, no. 2, pp. 747-760, Feb 2019, doi: 10.1364/BOE.10.000747.

[6] V. C. Torres, C. Li, Y. He, L. Sinha, G. Papavasiliou, H. A. Sattar, J. G. Brankov, and K. M. Tichauer, "Angular restriction fluorescence optical projection tomography to localize micrometastases in lymph nodes," J Biomed Opt, vol. 24, no. 11, pp. 1-4, 11 2019.

[7] V. C. Torres, C. Li, W. Zhou, J. G. Brankov, and K. M. Tichauer, “Characterization of an angular domain fluorescence optical projection tomography system for mesoscopic lymph node imaging,” Appl. Opt. 60(1), 135–146 (2021).
[8] K. Jun and S. Yoon, "Alignment Solution for CT Image Reconstruction using Fixed Point and Virtual Rotation Axis," Sci Rep, vol. 7, p. 41218, 01 2017, doi: 10.1038/srep41218.
[9] J. R. Walls, J. G. Sled, J. Sharpe, and R. M. Henkelman, "Correction of artefacts in optical projection tomography," Phys Med Biol, vol. 50, no. 19, pp. 4645-65, Oct 2005, doi: 10.1088/0031-9155/50/19/015.